International Symposium
On Turbulence and Shear Flow
Phenomena (TSFP-8)
August 28 - 30, 2013 Poitiers, France

PASSIVE FLOW CONTROL OF SHOCK-WAVE/TURBULENT-BOUNDARY-LAYER-INTERACTIONS USING MICRO VORTEX GENERATORS

Bernd Budich, Vito Pasquariello, Muzio Grilli and Stefan Hickel
Institute of Aerodynamics and Fluid Mechanics
Technische Universität München
Boltzmannstr. 15, D-85748 Garching, Germany
bernd.budich@tum.de

ABSTRACT

We evaluate the suitability of micro vortex generators for the passive flow control of shock-wave/turbulent boundary layer interactions. For this purpose, implicit large eddy simulations using the adaptive local deconvolution method are performed. The flow configuration consists of an oblique shock with deflection angle $\beta = 9.5°$, impinging on a turbulent boundary layer at $\mathrm{Ma}_\infty = 2.31$ and $\mathrm{Re} = 67.4 \cdot 10^3$. Analysis focuses on the assessment of the relative displacement between the control devices and the shock system, the complex flow structure behind the devices and the low-frequent motions of the separated region.

INTRODUCTION

Interactions of shock waves with turbulent boundary layers (SWBLI) can be encountered in virtually every high speed application, including engine intakes, turbomachinery or rocket engines. It is well known that shock induced flow separation is followed by severe energy losses and flow distortion degrading overall system performance (Babinsky *et al.*, 2009; Lin, 2002). Additionally, substantial thermal and pressure loads result from the interaction. In conjunction with their highly unsteady nature, SWBLI are of major concern also for the structural integrity and life time of high speed vehicles.

In order to address these issues, control devices can be deployed (Délery, 1985). Here, we focus on passive flow control using vortex generators (VGs), which rank among the most promising approaches to boundary layer control (Lin, 2002). Placed upstream of the interaction, these devices induce a pair of counter-rotating, longitudinal vortices that energize the boundary layer flow within their wake.

A valuable modification of conventional-type VGs are micro vortex generators (μVGs) possessing a device height of $h^{VG} \ll \delta_0$, with δ_0 being the 99%-boundary layer thickness. Due to their smaller height, exposure to lower fluid velocities, and reduced surface as well as cross-sectional areas, μVGs result in substantially lower parasitic losses and flow distortion while still efficiently increasing resistance against flow separation (Lin, 2002). However, relative placement to the separated region is crucial as dissipation and de-correlation of the vortex pair is of concern.

The considered flat plate turbulent boundary layer (TBL) is characterized by a free-stream Mach number $\mathrm{Ma}_\infty = 2.31$ and Reynolds number $\mathrm{Re}_\delta = 67.4 \cdot 10^3$, based on the reference boundary layer thickness $\delta_0^{ref} = 12.64\,\mathrm{mm}$, located at $8\,\delta_0^{ref}$ upstream of the theoretical inviscid impingement point (IP). The incident shock deflects the undisturbed flow by $\beta = 9.5°$. The employed wedge-shaped μVGs, see Fig. 1, possess an opening angle of 24°. The device's tip is located within the logarithmic region of the TBL ($h^{VG} = 0.2\,\delta_0^{ref} \approx 180\,l^+$), spanwise spacing is $s^{VG} = 1.6\,\delta_0^{ref}$.

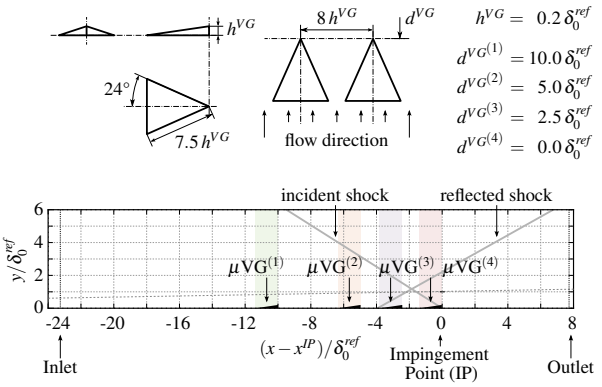

Figure 1: Geometry and placement of μVGs and dimensions of the numerical domain.

We consider four control configurations, μVG$^{(1)}$ – μVG$^{(4)}$, differing in the distance d^{VG} of the devices to the IP, as also sketched in Fig. 1. While μVG$^{(1)}$ is located well ahead of the shock system, μVG$^{(2)}$ is placed immediately upstream of the separation point. Furthermore, in order to investigate the effect of a possible misalignment, which could occur during transient processes or at off-design conditions, devices μVG$^{(3)}$ and μVG$^{(4)}$ are positioned within the separation bubble and directly at the IP, respectively.

The goal of the present study is to assess the impact of the control devices on the SWBLI. After outlining the numerical approach in the next section, the study subsequently focuses on analyzing the different regions of the flow. At first, the upstream TBL is examined. The baseline case without control serves for validating our method. Comparisons with the control cases subsequently demonstrate the influence of the devices on the flow conditions upstream of the SWBLI. Furthermore, time-averaged statistics of the interaction zone will be considered in detail for all setups. Examination of the wake behind μVG$^{(1)}$ and μVG$^{(2)}$ gives insight into the altered incoming flow structures. Finally, effects on the dynamics of the shock system are analyzed.

METHODOLOGY

We solve the three-dimensional, compressible Navier-Stokes equations in conservative, dimensionless form using an implicit large-eddy-simulation (ILES) on a Cartesian grid. For the fluid, an ideal gas assumption in conjunction with Sutherland's law for temperature-viscosity dependence is utilized. While the diffusive fluxes are computed using a 2nd-order central differencing scheme, the compressible adaptive local deconvolution method (ALDM) is applied for the convective fluxes. ALDM is based on a finite-volume scheme with a non-linear, solution-adaptive deconvolution operator (Hickel & Larsson, 2009). Time-integration is achieved by an explicit 3rd-order Runge-Kutta-scheme. The rigid body of the VGs is described by a conservative immersed boundary method (IBM, see Grilli *et al.*, 2009).

The dimensions of the numerical domain are $L_x \times L_y \times L_z = 31.08 \times 6.00 \times 1.6\ \delta_0^{ref}$ (in streamwise, wall-normal and spanwise direction, respectively), which is identical for all computations. The Cartesian grid consists of $N_x \times N_y \times N_z = 800 \times 180 \times 120 = 17.3 \cdot 10^6$ cells. The grid resolution in wall units is $\Delta x^+ = 35.73$ and $\Delta z^+ = 12.26$, with a minimum cell height of $\Delta y^+_{\min} \leq 1.38$.

The flat plate is modeled as no-slip and adiabatic wall. An essentially non-reflecting boundary condition based on Riemann invariants is used on the top, where the incident oblique shock is introduced using the Rankine-Hugoniot relations. In spanwise direction, periodic conditions are applied and linear extrapolation is used at the outlet. For generating the turbulent inflow signal, a digital filter (DF) technique is employed following the approach of Klein *et al.* (2003). This approach matches 1st- and 2nd-order statistics and moments of the TBL and ensures that no artificial correlations are introduced within the domain. The latter aspect is crucial for this investigation, as to avoid any interference with the low-frequency dynamics of the shock system.

For the statistics, samples with a temporal resolution of $1 \cdot 10^{-2}\ \delta_0/u_\infty$ are collected. The baseline and μVG$^{(1)}$ case have been run for an extended time of ≈ 60 flow-through times (FTTs, 1 FTT $= L_x/u_\infty$) while cases μVG$^{(2)}$ – μVG$^{(4)}$ span a run-time of 20 FTTs. In order to perform low-frequency analyses of the shock motion for the baseline and μVG$^{(1)}$, also the wall pressure signal was recorded for these cases (see below for details).

RESULTS

Upstream Turbulent Boundary Layer

The characteristics of the incoming TBL are pivotal to the formation and dynamics of the SWBLI. Therefore, precursor simulations have been carried out in order to assess the transition length necessary by the DF inflow boundary condition, domain dimensions as well as the numerical grid.

It was found that the DF technique generates a transient of about $10\,\delta_0^{ref}$ where modeling errors decay and a fully turbulent profile develops, providing sufficient distance to the regions of interest. Additionally, two-point auto-correlation functions in the spanwise and streamwise directions for the density, pressure and velocity components have been analyzed (omitted here for brevity), ensuring that the spanwise domain extent is large enough and that no artificial correlations are introduced by the inflow condition.

A comparison of the obtained TBL profile with reference data is given in Fig. 2. The streamwise position was chosen to be $15.63\,\delta_0^{ref}$ upstream of the IP, in order to match $\mathrm{Re}_\tau = 900$ from the DNS of Pirozzoli & Bernardini (2011). The van-Driest-transformed velocity profile in

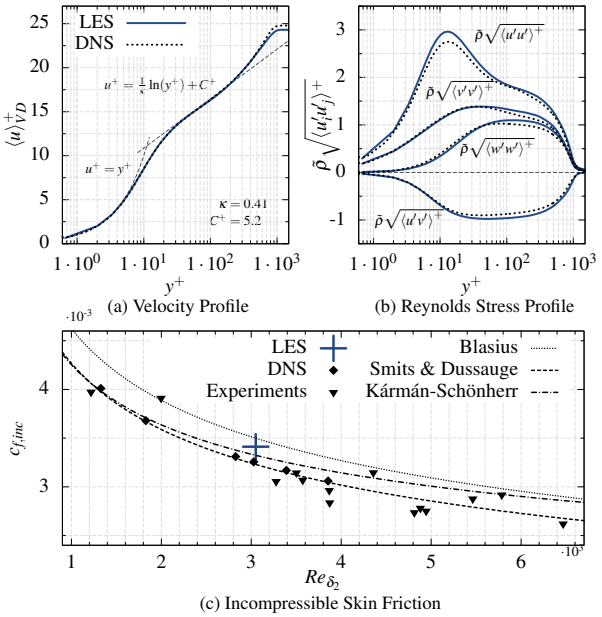

Figure 2: Characteristics of the incoming TBL at reference station $Re_\tau = 900$. With $\langle u \rangle^+_{VD} = 1/u_\tau \int_0^{\langle u \rangle^+} \sqrt{\langle \rho \rangle / \rho_w}\, d\langle u \rangle^+$ and $\tilde{\rho}\sqrt{\langle u_i'u_j' \rangle^+} = \sqrt{\langle \rho \rangle / \rho_w}\sqrt{\langle u_i'u_j' \rangle / u_\tau^2}$. Note: LES data at Ma = 2.3, DNS data at Ma = 2.0. Refer to the text for references on the validation data.

inner-layer scaling $\langle u \rangle^+_{VD}$ shows excellent agreement with the logarithmic law of the wall and the reference DNS data, see Fig. 2a. Similarly, the compressibility-corrected profiles of the Reynolds stresses $\tilde{\rho}\sqrt{\langle u_i'u_j' \rangle^+}$ match closely the DNS data. For the same reference station, the incompressible skin friction $c_{f,inc}$ is reported in Fig. 2c, which has been obtained by applying the van-Driest-II transformation (see e.g. Pirozzoli *et al.*, 2004). Reference data is taken from the already mentioned DNS, experimental data stems from AGARDOgraph No. 223, see Fernholz & Finley (1977). In addition, analytical correlations of Blasius, Kármán-Schönherr (cf. Pirozzoli *et al.*, 2004) and of Smits & Dussauge (2006) are included.

As Fig. 2c demonstrates, the obtained value of $c_{f,inc}$ in the incoming TBL is in very good agreement with all references, which further validates our numerical model.

Alteration of Upstream Characteristics

Flow control changes the upstream TBL. For μVG$^{(1)}$, μVG$^{(2)}$ and the baseline, Fig. 3 reports the streamwise evolution of the integral properties of the TBL, i.e. δ_0, the incompressible thicknesses $\delta_{1,inc}$, $\delta_{2,inc}$ and the shape factor $H_{12,inc}$, averaged in time and the spanwise direction.

All thickness measures locally increase above the control devices, due to their displacement effect. For μVG$^{(1)}$, placed further upstream, the thickness remains elevated compared to the baseline until the separation point. Simultaneously, for the same wedge, the shape factor is decreased by about 4%, indicating that the averaged velocity profile is profoundly energized in the near-wall region due to the mixing induced by the vortex pair. However, the mixing requires a length of about $2\,\delta_0^{ref}$ to develop its full effect on the shape factor. Therefore, and due to the presence of a wake region immediately behind the control devices, $H_{12,inc}$ is in contrast increased for μVG$^{(2)}$ in front of the SWBLI.

Additionally, we find that the sub-sonic region of the TBL is decreased by 12% for μVG$^{(1)}$ and 33% for μVG$^{(2)}$

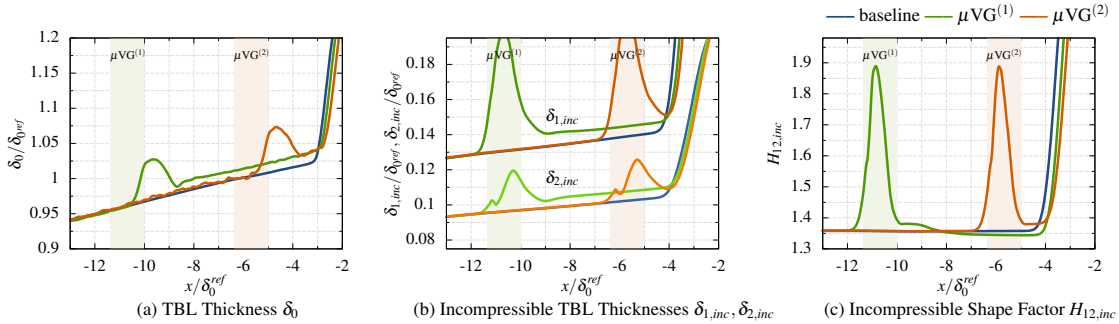

(a) TBL Thickness δ_0 (b) Incompressible TBL Thicknesses $\delta_{1,inc}, \delta_{2,inc}$ (c) Incompressible Shape Factor $H_{12,inc}$

Figure 3: Integral upstream boundary layer characteristics.

just before the flow separates. This effectively attenuates the upstream influence of the adverse pressure gradient, which plays a key role for the development and the extent of the interaction zone, see e.g. Délery (1985).

Alongside these spatially averaged properties, it should be noted that the μVGs induce significant variations within the upstream TBL in spanwise direction. As such, the shape factor is locally decreased by up to 10% compared to the baseline at positions of $\pm 0.2\,\delta_0^{ref}$ around the symmetry plane. Another illustration of these deviations from the spatial mean provides the local skin friction coefficient on the wall, shown in Fig. 4 for $\mu\mathrm{VG}^{(1)}$ and $\mu\mathrm{VG}^{(2)}$. Iso-lines of $c_f = 0$ mark the spatial extent of reversed flow, dashed lines denote the corresponding size for the baseline case. Within the vicinity of the wedges, as expected, the patterns of c_f closely resemble each other and show the typical footprint of a vortex pair, intensifying the friction lateral to the devices. The value of c_f is locally doubled, compared to the uncontrolled case. Similar structures were obtained experimentally by Babinsky *et al.* (2009) when investigating μVGs with a device height of $h^{VG} \approx 0.33\,\delta_0$. During their subsequent convection downstream, the vortices leave traces of increased c_f on the wall. Even for $\mu\mathrm{VG}^{(1)}$, this is perceptible until separation onset. The maxima of c_f are located at $\pm 1.3\,h^{VG}$ off the median plane.

Another aspect highlighted by Fig. 4, is the pronounced spanwise variation of the separated region, which is discussed in context of the interaction zone in the next section.

Due to their small height, the influence of the μVGs on the upstream conditions is restricted to the near-wall region. In the next section it becomes apparent hat weak compression waves develop above the devices. However, flow properties outside the TBL remain almost unchanged, as subsequent expansions return the free stream to its initial state. The Mach number, flow direction as well as total and static pressures vary by less than 3% upstream of the incident shock, leaving the compression strength almost unmodified. Therefore, the impact of the μVGs on the interaction region, as described below, essentially relies on the alteration of the inner part of the TBL, distinguishing them from conventional-type VGs.

Interaction Zone

The iso-lines of $c_f = 0$ shown in Fig. 4 visualize the topology of the separation on the wall-plane. Upon the influence of devices $\mu\mathrm{VG}^{(1)}$ and $\mu\mathrm{VG}^{(2)}$, the separation and reattachment line both exhibit a substantial spanwise variation, in contrast to the baseline. Even though direct interaction between the vortices and the shock is not to be expected for $\mu\mathrm{VG}^{(1)}$, separation onset is delayed locally by about $1.3\,\delta_0^{ref}$. For $\mu\mathrm{VG}^{(2)}$, the separation line is partially displaced downstream by almost $2\,\delta_0^{ref}$. Therefore, it is conjectured that the vortices for this configuration penetrates through the reflected shock into the interaction zone.

The spatial and time-averaged skin friction coefficient as well as wall pressure within the interaction region are shown in Fig. 5. The pre-interaction wedges lead to an elevated level of c_f within their wake, see Fig. 5a. Accordingly, this substantiates the presence of a steeper velocity gradient and thus fuller velocity profile, not only locally but for the spatial mean, as already indicated by the inspection of $H_{12,inc}$. This is consistent with the downstream displacement of the separation point. Simultaneously, reattachment shifts upstream under the presence of the wedges. The corresponding wall pressure, while remaining unchanged upstream, exhibits a steeper profile within the SWBLI. Pressure rise happens later because of the reduced upstream propagation of the adverse gradient through the remarkably reduced subsonic region of the TBL, as already discussed.

Table 1: Integral properties of the interaction zone.

	L_{sep}/δ_0^{ref}	L_{int}/δ_0^{ref}	H_{sep}/δ_0^{ref}	L_{sep}/H_{sep}
baseline	4.711	4.373	0.189	23.09
$\mu\mathrm{VG}^{(1)}$	4.337	4.185	0.169	24.82
$\mu\mathrm{VG}^{(2)}$	3.834	4.054	0.133	30.51
$\mu\mathrm{VG}^{(3)}$	5.154	4.551	0.181	28.41
$\mu\mathrm{VG}^{(4)}$	4.749	4.357	0.181	26.24

L_{sep}: streamwise extent of region with negative c_f
L_{int}: distance between reflected shock foot mean position and IP
H_{sep}: maximum wall-normal extent of $u = 0$ contour line

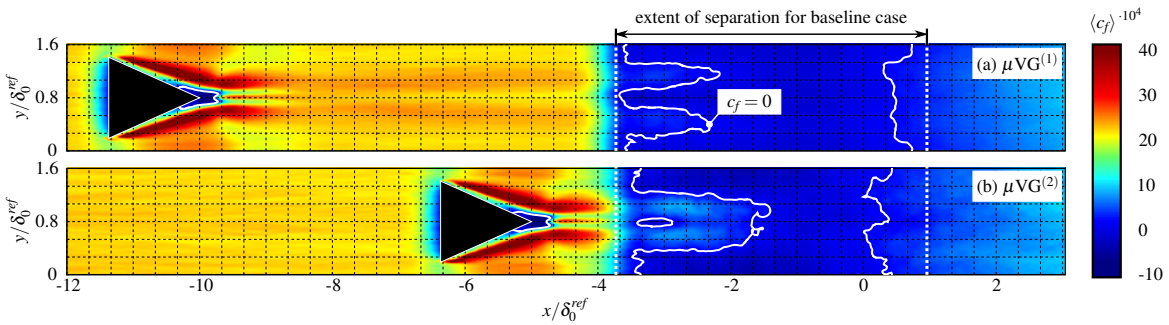

Figure 4: Skin friction coefficient c_f on the wall-plane ($y = 0$).

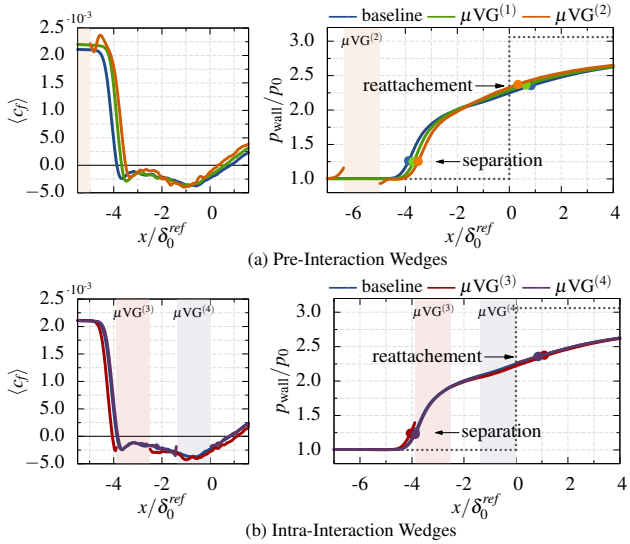

(a) Pre-Interaction Wedges

(b) Intra-Interaction Wedges

Figure 5: Skin friction coefficient c_f and wall pressure p_{wall}/p_0 within the interaction region.

The weak pressure plateau of the baseline completely disappears for the control cases. For the intra-interaction wedges, on the other hand, c_f and p_{wall} in Fig. 5b show only few deviations from the baseline. For μVG$^{(3)}$, the separation point is displaced upstream and the pressure plateau is slightly more pronounced. Results for case μVG$^{(4)}$ yet again coincide mostly with the baseline case for these quantities.

A summary of the interaction zone integral parameters is included in Tab. 1. Both upstream ramps decrease the extent of the interaction. The highest impact shows μVG$^{(2)}$, decreasing L_{sep} by 18%. Even larger is the effect on the height of the reverse-flow region H_{sep}, which is reduced by nearly 30%, resulting in a considerably modified bubble aspect ratio L_{sep}/H_{sep} and blocking factor for the channel. The opposite effect is found for μVG$^{(3)}$. Both L_{sep} and H_{sep} are raised by 18% and 40%, respectively. μVG$^{(4)}$ yields almost identical quantities as the uncontrolled case.

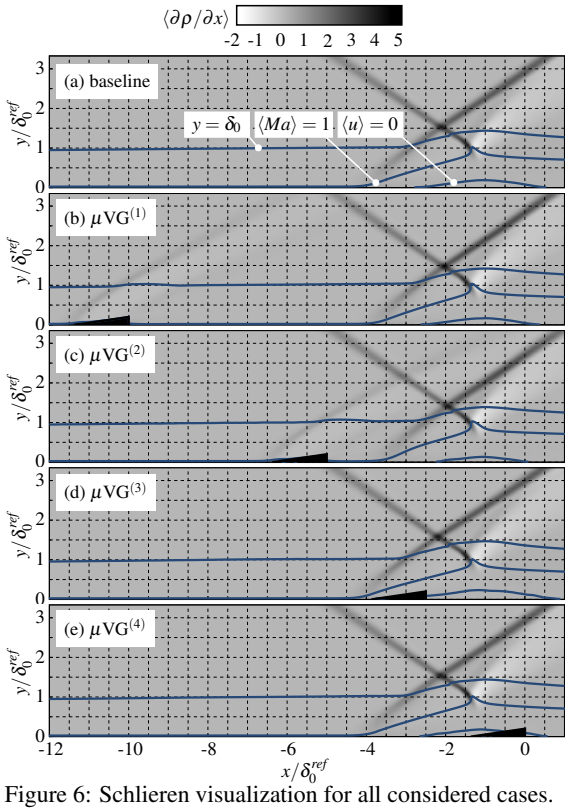

Figure 6: Schlieren visualization for all considered cases.

For better visualization of the above findings, numerical schlieren images for the baseline and all control cases are provided in Figs. 6a - 6e. The uncontrolled case exhibits the classical flow configuration of a SWBLI. By comparing the flow fields, the upstream introduction of the μVGs delays flow separation and reduces the interaction zone in both its streamwise and wall-normal extent. Furthermore, the sonic line for these cases lifts away from the wall at a position further downstream but is subsequently steeper inclined. This corroborates the fact that the upstream influence of the adverse pressure gradient is indeed reduced. Overall, wedge μVG$^{(2)}$ has a larger influence on these aspects compared to μVG$^{(1)}$, which is in agreement with the above findings. In contrast, the two intra-interaction wedges μVG$^{(3)}$ and μVG$^{(4)}$ lead to an increased bubble size. As expected, the placement within the highly unsteady and turbulent separated region suppresses their ability to induce a pair of coherent vortices. Moreover, the flow displacement and subsequent wake yet facilitate separation.

Figs. 7a - 7e show time-averaged visualizations of the Reynolds shear stress $-\langle u'v' \rangle$ for all configurations. The baseline clearly exhibits a region of increased turbulence just behind the reflected shock, which is characteristic for the shear layer above the separation. Originating at the reflected shock foot, it is inclined at an angle of 11°. The turbulence kinetic energy TKE $= 1/2\,\langle u_i' u_i' \rangle$ (not shown) attains a peak value within this shear layer, which is higher than in the undisturbed TBL by a factor of 2.8, being in agreement with a DNS of Pirozzoli & Grasso (2006) at Ma $= 2.25$ and comparable shock strength. This amplification is decreased for μVG$^{(1)}$ and μVG$^{(3)}$ by ca. 7% and 12%, respectively, while remaining unchanged for μVG$^{(2)}$ and μVG$^{(4)}$.

In addition, Figs. 7a - 7e visualize the flapping motion of the reflected shock, which extends beyond the TBL well into the free stream. These motions are attenuated for case μVG$^{(1)}$ and μVG$^{(3)}$. However, the opposite situation of an amplified shock motion is observed for μVG$^{(2)}$, while the level of shock oscillations is almost unchanged for μVG$^{(4)}$, following the same trends as described above.

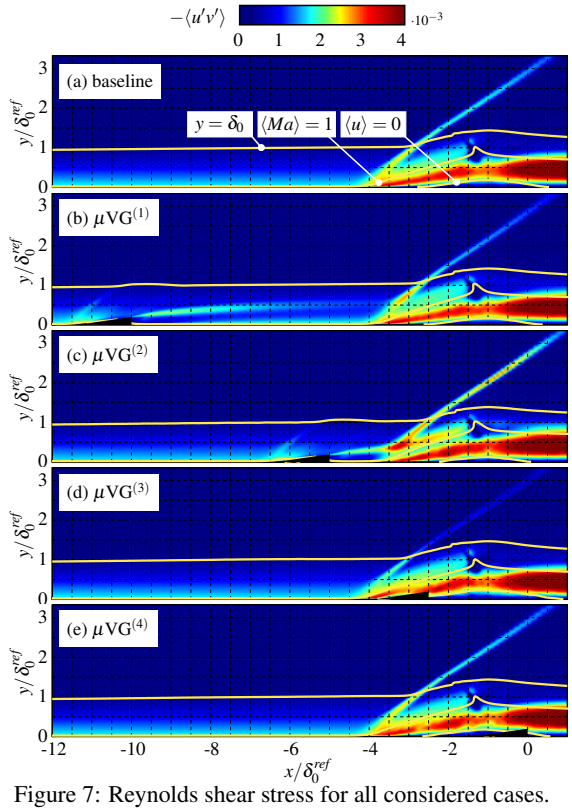

Figure 7: Reynolds shear stress for all considered cases.

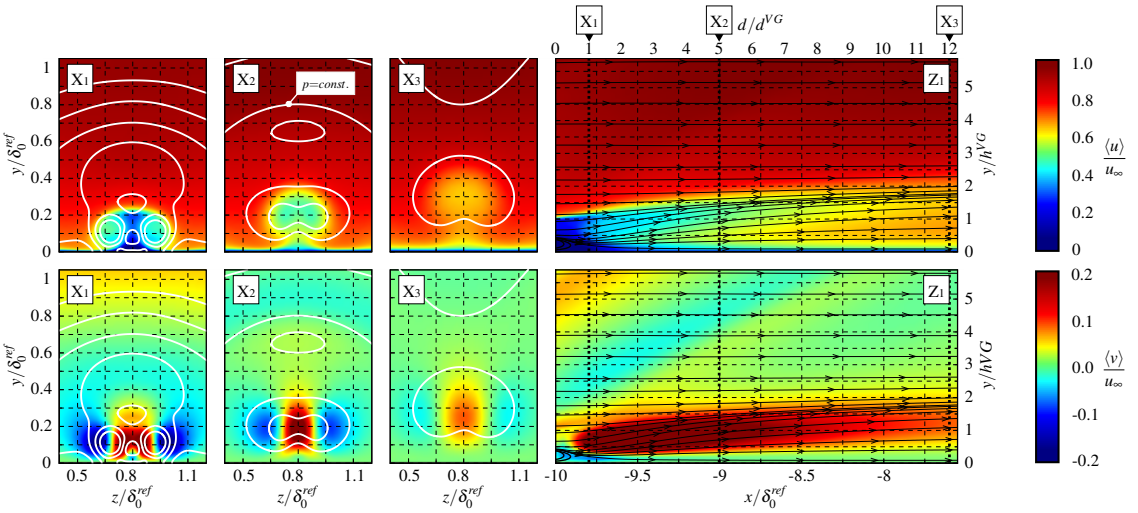

Figure 8: Axial and wall-normal velocity components $\langle u\rangle/u_\infty$ and $\langle v\rangle/u_\infty$ on cut-planes within the wake of wedge μVG$^{(1)}$.

Within the wake of both upstream wedges, a region of increased Reynolds stresses has its source at the tip of the devices. Stemming from the intense mixing induced by the vortex pair, the maximum can be found at $y \gtrsim 180\,l^+$, i.e. within the logarithmic region of the TBL. Even for μVG$^{(1)}$, located further upstream, this higher turbulence level is noticeable just in front of the interaction region. Consequently, it gets further augmented by the reflected shock for these two cases. Being more pronounced for μVG$^{(2)}$due to the device's proximity, this leads to a second maximum of turbulent fluctuations situated above the original shear layer.

Induced Vortex Pair

To analyze the induced vortex pair in more detail for the upstream wedges, time-wise averaged axial and wall-normal velocities $\langle u\rangle/u_\infty$ as well as $\langle v\rangle/u_\infty$ behind μVG$^{(1)}$ are shown in Fig. 8 on planes perpendicular (X$_1$-X$_3$, at a distance of $d = 1, 5, 12\,h^{VG}$ behind the wedge) and parallel to the flow (Z$_1$, symmetry plane $z = 0.8\,\delta_0^{ref}$). Also included are streamlines and iso-lines of pressure.

The vortex cores appear as low-pressure regions on planes X$_1$-X$_3$. The vortex system induces a net velocity directed away from the wall and thus results in an upward lift of these cores. Ascent happens almost linearly, being in agreement with experimental findings of Sun *et al.* (2012).

Immediately downstream of the wedge, a mushroom-shaped region of momemtum deficit is attached, resulting from the upwash in between the vortex pair and the corresponding downwash on either flank, as depicted by $\langle v\rangle/u_\infty$. On the median plane, it reaches values of more than 20% of the freestream axial velocity. This yields a distinct deficit region on the symmetry plane persisting several TBL thicknesses. The downwash simultaneously energizes the TBL on the outside of the vortices, apparently with a larger net effect on the spatial average. Despite its coherence, this redistribution of momentum is restricted to the inner part of the TBL and has no noticeable influence at $y \gtrsim 0.5\,\delta_0^{ref}$.

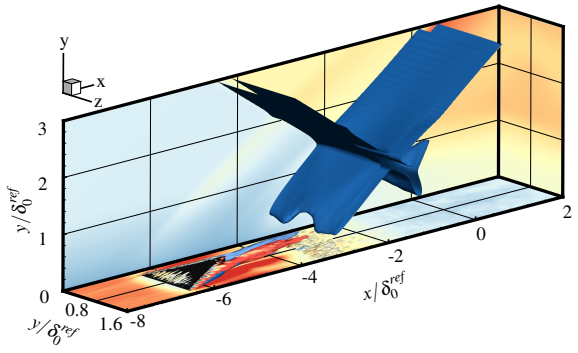

Figure 9: Visualization of the interaction region controlled by μVG$^{(2)}$(iso-surfaces of $Q = 1.5$ and $\partial p/\partial x = 0.17$).

The three-dimensional structure of the vortex pair behind μVG$^{(2)}$ and its effect on the shock system is shown in Fig. 9. Iso-contours of the Q-criterion $Q = 1.5$, colored by axial vorticity ω_x, highlight how the two distinct, counter-rotating vortices develop on either side of the wedge. While lifting away from the wall, they are consecutively convected towards the shock system, which is visualized in Fig. 9 by iso-surfaces of $\partial p/\partial x = 0.17$. As already discussed in the context of Fig. 4, the vortices penetrate the reflected shock at its base. Additionally, at greater wall-normal distance, the shock exhibits a noticeable axial displacement that varies in spanwise direction.

Low-Frequency Shock Motion

It is well known from various numerical and experimental investigations (see e.g Touber & Sandham, 2009; Dupont *et al.*, 2006, and references therein), that the reflected shock performs a distinct, low-frequent oscillation around its spatial mean. The characteristic frequency of this motion is magnitudes lower than that of the TBL. Among others, Dupont *et al.* (2006) motivate L_{int} as length scale for obtaining a Strouhal-number $\mathrm{St}_{LFC} = fL_{int}/u_\infty$, which was found to lie within the range $0.02 \lesssim \mathrm{St}_{LFC} \lesssim 0.04$, independent of the configuration under investigation.

Here, the unsteady shock motion for the baseline and for μVG$^{(1)}$ is analyzed by recording the wall pressure signal on the mid-plane. Pressure probes, spaced apart by $\Delta x = 0.05\,\delta_0^{ref}$, cover the range $-10 \le x/\delta_0^{ref} \le 6$. With a temporal resolution of $0.026\,\delta_0^{ref}/u_\infty$, a time-span of 53 FTTs (baseline) and 44 FTTs (μVG$^{(1)}$) is monitored, thus resolving Strouhal-numbers of $7.5\cdot10^{-4} \lesssim \mathrm{St}_\delta \lesssim 18$.

Results of the analyses are provided in Fig. 10 in terms of the pre-multiplied Power Spectral Density (PSD) of the pressure signal. For the baseline case, Fig. 10a, four regions ①-④ can be identified. The upstream region ① is characterized by $\mathrm{St}_\delta \approx 1$ as to be expected for a flat plate TBL. In ②, the reflected shock motion becomes apparent by an elevated level of the spectrum at the considerably lower frequency $f_{LFC} = 0.006\,u_\infty/\delta_0^{ref}$. The associated interaction-length Strouhal-number $\mathrm{St}_{LFC} = 0.026$ is in excellent agree-

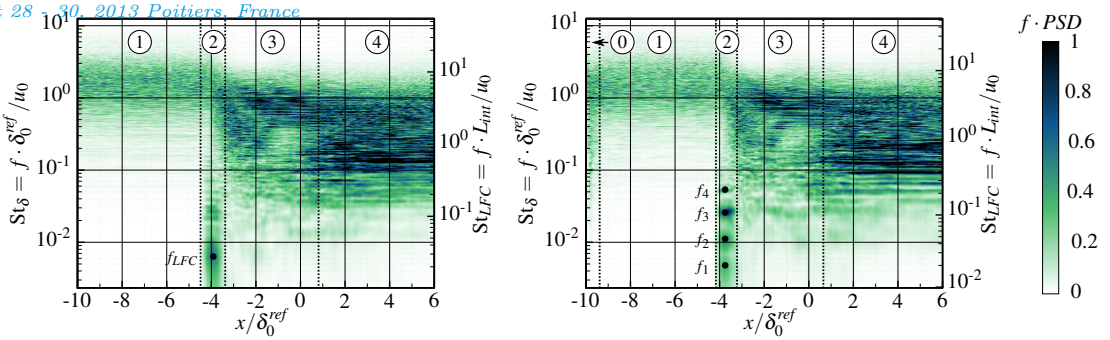

(a) Baseline case

(b) Controlled case μVG$^{(1)}$

Figure 10: Premultiplied, weighted PSD ($f \cdot PSD / \int f \cdot PSD \, df$) of the wall-pressure signal for probes located on the mid-plane.

ment with previous experiments (Dupont *et al.*, 2006). The simulation thus covers 10 cycles at this frequency. The spatial extent of region ② is connected to the axial excursion L_{ex} of the reflected shock. We found $L_{ex} \approx 1.2\,\delta_0^{ref}$ for the baseline, in agreement with literature values. The reversed flow within region ③ is again dominated by higher frequencies. However, due to the growing shear layer behind the reflected shock, a gradual shift towards lower values of St_δ can be observed. Finally, the relaxation region ④ is characterized by a broadband spectrum at frequencies lower than within ① as the TBL thickens across the interaction.

Placing μVG$^{(1)}$ within the flow, low-frequency content is generated just downstream of the wedges by the vortex shedding at the device's trailing edge, indicated in Fig. 10b as region ⓪. This immediate influence is quickly attenuated, as the PSD within ① remains almost unaltered compared to the baseline. Also, regions ③ and ④ show similar characteristics. However, the dynamic behavior within ② is changed considerably. The distinctive peak in the baseline spectrum is replaced by a series of maxima at almost harmonic frequencies $f_i = (0.0046, 0.01149, 0.0253, 0.0506)\, u_\infty / \delta_0^{ref}$, $f_1 < f_{LFC} < f_2$.

Hence, it is conjectured that resonance issues can be addressed with the investigated control devices. Moreover, the amplitude of the unscaled PSD for μVG$^{(1)}$ is lower than for the baseline, indicating the weakened strength of the oscillations. Furthermore, as the excursion L_{ex} is reduced by 25%, the wall area exposed to most energetic pressure variations is minimized. This is in agreement with the lessened fluctuations (see again Fig. 7a) of the reflected shock.

CONCLUSION

The interaction between an oblique shock with $\beta = 9.5°$ and a turbulent boundary layer at $Ma = 2.31$ and $Re = 67.4 \cdot 10^3$ has been investigated and the effectiveness of passive flow control using wedge-shaped micro vortex generators (μVGs) has been assessed.

It has been found that a significant reduction of the interaction's spatial extent can be achieved. Placing the μVGs closely upstream the reflected shock constitutes the most favorable configuration. This can be accredited to a combined positive effect of energizing the logarithmic region of the TBL, a reduction of upstream propagation of the adverse pressure gradient and an increase of turbulence intensity.

In contrast, a misalignment of the shock system only leads to a restricted separation growth. It can be concluded that overall system performance is not excessively deteriorated at off-design conditions. Furthermore, the freestream is only slightly changed and almost no additional loss in total pressure is introduced into the system. These findings underline the efficacy of the μVGs compared to conventionally-sized devices.

Moreover, control also alters the shock oscillations, regarding their frequency content, amplitude and excursion area. Clearly being connected to material stress and fatigue, μVGs can thus be employed to address these aspects.

References

Babinsky, H., Li, Y. & Pitt Ford, C.W. 2009 Microramp Control of Supersonic Oblique Shock-Wave/Boundary-Layer Interactions. *AIAA Journal* **47** (3), 668–675.

Délery, J.M. 1985 Shock Wave/Turbulent Boundary Layer Interaction and its Control. *Progress in Aerospace Sciences* **22**, 209–280.

Dupont, P., Haddad, C. & Debiève, J.-F. 2006 Space and time organization in a shock-induced separated boundary layer. *Journal of Fluid Mechanics* **559**, 255–277.

Fernholz, H.H. & Finley, P.J. 1977 *A Critical Compilation of Compressible Turbulent Boundary Layer Data* .

Grilli, M., Hickel, S., Hu, X.Y. & Adams, N.A. 2009 Conservative immersed boundary method for compressible flows. In *Academy Colloquium on Immersed Boundary Methods: Current Status and Future Research Directions*. Amsterdam.

Hickel, S. & Larsson, J. 2009 On implicit turbulence modeling for LES of compressible flows. In *Advances in Turbulence XII* (ed. Bruno Eckhardt), *Springer Proceedings in Physics*, vol. 132, pp. 873–875. Springer.

Klein, M., Sadiki, A. & Janicka, J. 2003 A digital filter based generation of inflow data for spatially developing direct numerical or large eddy simulations. *Journal of Computational Physics* **186** (2), 652–665.

Lin, J.C. 2002 Review of research on low-profile vortex generators to control boundary-layer separation. *Progress in Aerospace Sciences* **38** (4-5), 389–420.

Pirozzoli, S. & Bernardini, M. 2011 Turbulence in supersonic boundary layers at moderate Reynolds number. *Journal of Fluid Mechanics* **688**, 120–168.

Pirozzoli, S. & Grasso, F. 2006 Direct numerical simulation of impinging shock wave/turbulent boundary layer interaction at M = 2.25. *Physics of Fluids* **18** (6), 065113.

Pirozzoli, S., Grasso, F. & Gatski, T.B. 2004 DNS and analysis of a spatially evolving supersonic turbulent boundary layer at M= 2.25. *Physics of Fluids* **16** (3), 530–545.

Smits, A.J. & Dussauge, J.-P. 2006 *Turbulent Shear Layers in Supersonic Flow*, 2nd edn. Springer.

Sun, Z., Schrijer, F.F. J., Scarano, F. & van Oudheusden, B.W. 2012 The three-dimensional flow organization past a micro-ramp in a supersonic boundary layer. *Physics of Fluids* **24** (5), 055105.

Touber, E. & Sandham, N.D. 2009 Large-eddy simulation of low-frequency unsteadiness in a turbulent shock-induced separation bubble. *Theoretical and Computational Fluid Dynamics* **23** (2), 79–107.